GEOPHYSICS

Surface parameters and bedrock properties covary across a mountainous watershed: Insights from machine learning and geophysics

Sebastian Uhlemann[1]*, Baptiste Dafflon[1], Haruko Murakami Wainwright[1]†, Kenneth Hurst Williams[1,2], Burke Minsley[3], Katrina Zamudio[3], Bradley Carr[4], Nicola Falco[1], Craig Ulrich[1], Susan Hubbard[1]

Bedrock property quantification is critical for predicting the hydrological response of watersheds to climate disturbances. Estimating bedrock hydraulic properties over watershed scales is inherently difficult, particularly in fracture-dominated regions. Our analysis tests the covariability of above- and belowground features on a watershed scale, by linking borehole geophysical data, near-surface geophysics, and remote sensing data. We use machine learning to quantify the relationships between bedrock geophysical/hydrological properties and geomorphological/vegetation indices and show that machine learning relationships can estimate most of their covariability. Although we can predict the electrical resistivity variation across the watershed, regions of lower variability in the input parameters are shown to provide better estimates, indicating a limitation of commonly applied geomorphological models. Our results emphasize that such an integrated approach can be used to derive detailed bedrock characteristics, allowing for identification of small-scale variations across an entire watershed that may be critical to assess the impact of disturbances on hydrological systems.

INTRODUCTION

Subsurface structure and property distributions—from soil to the unweathered bedrock—are one of the biggest uncertainties in the prediction of hydrology and watershed processes (*1*). Subsurface porosity and permeability govern the storage and flow of water and nutrients (*1*–*3*), control subsurface-surface interactions (*4*–*6*), and buffer climatic variability and biogeochemical dynamics (*7*). However, subsurface characterization is difficult using conventional wellbore approaches. These intrusive investigations can shed light on the physical parameters of the regolith and bedrock, thereby quantifying hydrological flow and bedrock weathering and fracturing parameters (*8*, *9*). However, the derived data are representative of the properties in the immediate vicinity of the boreholes only, and upscaling to estimate the variability at a watershed scale is challenging and fraught with high uncertainty. As a result, quantitative subsurface characterization has been mostly restricted to analyzing hillslopes along short transects [e.g., (*8*, *10*)] rather than across watershed scales [as highlighted in, e.g., (*7*)]. To develop a predictive understanding of watershed function, including climate change impacts on water and biogeochemical cycling, new approaches are needed to estimate watershed subsurface properties with sufficient accuracy and yet at length scales and over spatial extents relevant to such cycling.

While the importance of shallow bedrock properties on the functioning of watersheds and the ecosystem services that they provide has been highlighted in numerous studies [e.g., (*3*, *11*)], those bedrock properties are commonly neglected because of the difficulty associated with their characterization. Two key approaches have been used to mitigate this challenge. The first approach is the use of geophysical datasets, including their combination with wellbore data to characterize fracture systems in shallow, fractured hard rock environments (*12*–*14*), as well as their combination with hydrological modeling to estimate bedrock hydraulic properties and subsurface flow dynamics (*15*, *16*). Although these studies provide useful information with regard to bedrock hydraulic properties, they were mostly focused on site-scale, two-dimensional transects, and more recently, similar approaches are starting to be applied to estimate spatially extensive bedrock properties (*17*). The second key approach focuses on using spatially distributed proxy information. Recent work has focused on the use of geomorphological indices, such as slope angle, aspect, tectonic stress, and distance to streams, to estimate the thickness of the subsurface comprising soil and weathered rock, i.e., the thickness of the regolith (*18*–*22*). These models usually assume that crest-to-valley geomorphic processes are controlling the regolith thickness, rather than geological heterogeneity. While these approaches enable estimation of subsurface characteristics over watershed scales, they do not provide estimates of subsurface hydraulic properties, which are required to accurately predict groundwater flow and reactive transport (*23*). Characterization of hydrologic heterogeneity is particularly important for hard rock environments (i.e., crystalline igneous, metamorphic, and cemented carbonate and sedimentary rocks), which cover about 50% of Earth's land surface (*24*). In these environments, discontinuities (such as fractures or faults) or structural elements (such as fracture zones) are known to govern the hydrological response of fractured bedrock aquifers (*25*).

To fully understand the multidimensional variability of bedrock properties throughout a mountainous watershed, new approaches are required that can assess the spatial variability of hydraulic parameters (*26*, *27*) and ideally can take advantage of increasingly available, spatially distributed remote sensing datasets.

[1]Earth and Environmental Sciences Area, Lawrence Berkeley National Laboratory, Berkeley, CA 94720, USA. [2]Rocky Mountain Biological Laboratory, Gothic, CO 81224, USA. [3]Geology, Geophysics, and Geochemistry Science Center, U.S. Geological Survey, Denver, CO 80225, USA. [4]Department of Geology and Geophysics, University of Wyoming, Laramie, WY 82071, USA.
*Corresponding author. Email: suhlemann@lbl.gov
†Present address: Department of Nuclear Science and Engineering, Massachusetts Institute of Technology, Cambridge, MA 02139, USA.

The lack of studies addressing the spatial variability of subsurface properties throughout a watershed possibly has two reasons: (i) Many studies focus on specific process investigations, such as weathering, sediment transport, or nutrient cycling, which can be performed through focusing on a hillslope or subsystem, without the need for studying large-scale property variations; and (ii) appropriate data to scale plot observations to regional variability are scarce. Here, we present an integrated approach using measurements ranging from borehole and surface to airborne geophysical measurements. Recent developments in data inversion allow for the analysis of large airborne electromagnetic (AEM) datasets (*28*). AEM datasets use electromagnetic fields to measure the electrical response of the subsurface, which is used to derive depth-resolved electrical resistivities (*29*). The electrical resistivity of bedrock is mostly dependent on the formation's mineral composition, pore fluid content, and available pore space (*30*). For example, using AEM data, subsurface properties in Alaska over an area of about 300 km^2 have been estimated (*31*). Within the last few years, AEM surveys are covering increasingly larger areas at regional basin scales, as large as 140,000 km^2 (*32*), and are moving from predominantly flat areas [e.g., (*33*, *34*)] to mountainous environments (*35*–*37*). There is an increased effort to use AEM data to construct hydrological models from local to regional scales (*38*–*40*).

Our goal is to investigate covariability of bedrock geophysical properties, derived from an integrated analysis of borehole, surface and airborne geophysical methods, and geomorphological and vegetation indices, within a hard rock environment. Building on the findings of abovementioned geomorphological studies [e.g., (*22*)], we hypothesize that topographic and vegetation metrics covary with bedrock electrical resistivity on a watershed scale. We test this hypothesis by developing a machine learning model linking these metrics to AEM-derived shallow bedrock electrical resistivities and eventually to hydraulic properties. Because the electrical resistivity is an indirect measure of bedrock weathering, water saturation, and hydraulic and fracture properties, such a combination should provide an opportunity to scale the subsurface properties over the region to allow for a detailed parameterization of large-scale hydrological models. While many studies show the validity of geomorphological models for estimating regolith thickness and have proven the relationship between subsurface bedrock properties and surface expressions over hillslope scales, this is the first study that assesses bedrock property variability across multiple hillslopes over a large watershed.

This study makes use of data acquired in a mountainous system. Data were collected at the point and hillslope scales (e.g., core observations, borehole logs, and surface geophysical transects) to the watershed scale [e.g., airborne geophysics, light detection and ranging (LiDAR), and hyperspectral data] to estimate the variability of subsurface properties at the site (Fig. 1). We assume that variations in the subsurface electrical properties, as imaged by surface and airborne geophysical methods, are predominantly driven by variations

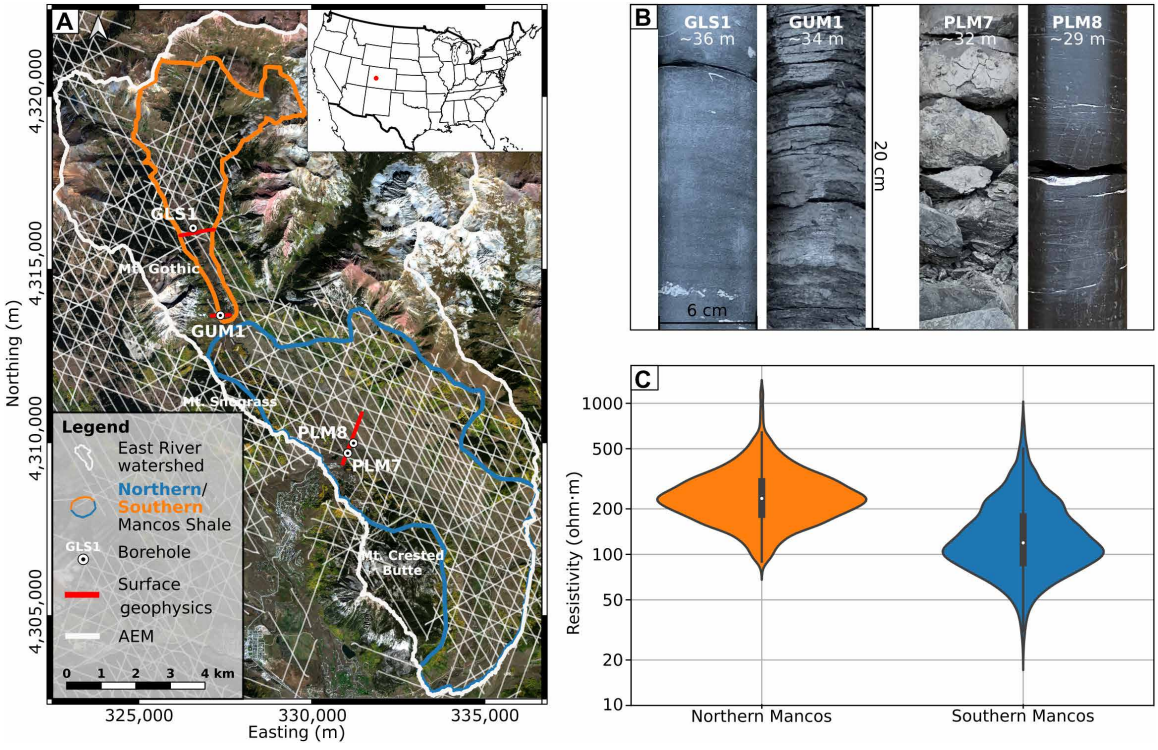

Fig. 1. Data inventory and large-scale characteristics of the study site. Overview map showing the location of boreholes, surface geophysical transects, and AEM (*35*) flight lines [(**A**), Universal Transverse Mercator (UTM) Zone 10N] on top of an aerial photograph (*71*). Also shown are the outline of the watershed and the area underlain by Mancos Shale. On the basis of the attributes shown in (B) and (C), the Mancos Shale is divided into a northern unit and a southern unit. Not shown here, the data inventory also includes LiDAR data and detailed vegetation classification using hyperspectral data (*69*). (**B**) Photographs of the Mancos Shale cores recovered from the boreholes, highlighting variability in Mancos Shale properties. Boreholes GLS1 and GUM1 are located in the upper part of the watershed, while PLM7 and PLM8 are located in the lower part (photo credit: Kenneth Williams, Lawrence Berkeley National Laboratory). (**C**) Resistivity distribution of the upper 20 m of the southern and northern Mancos Shale as obtained from the AEM data.

in lithology, the effective porosity, and fracture density or weathering of the underlying rock [e.g., (*41*)]. To eliminate the effect of varying lithology, we are focusing our analysis on the dominant lithological unit (Mancos Shale). Groundwater levels throughout the Mancos Shale unit have been observed to be shallow (<10 m), given the sensitivity of the AEM measurements variations in groundwater level are deemed to have negligible impact on the results. While borehole observations and near-surface geophysical data provide detailed information about soil, regolith, and bedrock properties at specific locations, airborne geophysical data give a spatially distributed, aggregated response of the regolith column across watershed scales, including small-scale features (fracture zones or biogeochemical hot spots) that are difficult to identify using sparse measurements. Although the resolutions of hillslope and remote sensing methods are different, we show here that they can be combined effectively to estimate bedrock parameters at resolutions of 20 m^2 across the 300-km^2 watershed.

This methodology is developed at and applied to the East River watershed, located close to Crested Butte, Colorado (Fig. 1A). The study area comprises an area of about 135 km^2, with a topographic relief of 1700 m and associated variability in vegetation, hydrology, and weather (*42*). The dominating vegetation community types, in order from low to high elevations, are sagebrush, aspen, spruce-fir, upland herb, and alpine assemblages. In this area, like in other mountainous areas, lithological and vegetation patterns are coincident (*43*). The geomorphology of the watershed is characterized by gentle to steep slopes, with an average slope angle of 25.5°, and is controlled by the bedrock type; while shale formations relate to open valleys, limestone formations tend to form sharp cliffs and granodiorite intrusions form rugged peaks (*44*). Surface deposits comprise rock glaciers, talus, landslide, and in the lower elevations lateral moraine deposits (*45*). The East River, being a previously glaciated subalpine system, is characterized by shallow down-valley gradients, heterogeneous floodplain sediments, and a channel morphology that ranges from high-energy mountain streams to low-energy meandering floodplains (*46*). The climate is continental subarctic, and stream discharge is snow-dominated, peaking in early June and receding through the summer and fall. Recent work has shown that deep groundwater flow, which is controlled by the bedrock properties, provides a substantial input to streamflow in this mountainous watershed (*47*). This shows that within this mountainous watershed, the bedrock provides major control on the critical zone, including vegetation patterns, geomorphological characteristics, and hydrological response, and hence supports our hypothesis.

The bedrock geology is dominated by Cretaceous Mancos Shale (accounting for >40% of the outcropping formations), with laccolith-shaped Oligocene intrusions of granodiorite, forming Mt. Crested Butte, Mt. Snodgrass, and Mt. Gothic. Mancos Shale is a gray to dark-gray marine shale, with a maximum thickness of 1500 m (*48*). It is a rock unit that formed during transgressive and regressive episodes of the Western Interior Seaway, resulting in minor facies of limestone, marlstone, bentonite, concretions, and sandstone beds (*49*). Mancos Shale is known to have generally low hydraulic conductivities, with higher values primarily associated with fracture zones (*50*). Shale is a rock of global importance; it is a critical geological unit for energy resources and also serves as a source for nutrients and geogenic contaminants (*51*, *52*). Outcropping mostly on the eastern side of the watershed are the Cretaceous Fort Hays Limestone and Dakota Sandstone, and Middle Pennsylvanian to lower Permian Maroon Formation. The area felt increased compressive stress during the Laramide orogeny, shown by emplacement of sills and thrust faults (*53*). Postglacial stress release after the Quaternary glaciation caused sackungen (*44*), which are slow, deep-seated gravitational slope deformations. The past and current-day extensional stress regime likely contributed to the formation of a complex network of fractures in East River watershed. While some of the fractures have been mapped using surface methods (*44*), others are likely hidden underneath thin Quaternary deposits. Because subsurface electrical properties are dependent on the bedrock type, we limit our analysis to areas underlain by Mancos Shale.

The East River watershed is representative of many headwater catchments of the Rocky Mountains, which provide ~85% of the streamflow of the Colorado River Basin and supply about 40 million people and 20,000 km^2 of agricultural land with water (*54*). While it is known that these alpine systems are sensitive to climate warming, the impact of climate change on their water supply is difficult to estimate (*55*). Understanding the bedrock properties of the East River watershed and the related feedback of environmental disturbances to groundwater will eventually help to improve downstream water management.

RESULTS

General bedrock and AEM resistivity characteristics

Four boreholes were drilled throughout the watershed, and core inspection and geophysical borehole logging were performed to characterize the vertical variability in bedrock properties (*56*). Two of the boreholes are located in the upper watershed (GLS1 and GUM1) and the other two are in the lower watershed (PLM7 and PLM8; Fig. 1A). At GLS1, the shale unit showed some minor fractures, mostly parallel to the bedding plane (approximately at 21-, 27-, and 33-m depth), and thin quartz veins; visual inspection (Fig. 1B) indicated that most of the ~51-m core is characterized by unfractured and homogeneous shale. At GUM1 (upper watershed), the recovered core showed horizontal, fine-scale fracturing along the bedding plane, which is attributed to mechanical stress induced by the intrusion of the nearby Mt. Gothic laccolith. Occasional subvertical fracturing is observed within the core. In the lower watershed, visual inspection of the PLM7 core revealed major brecciated fracture zones (>1 m thick) from the top of the borehole down to a depth of about 59 m, with intermittent up to 2-m-thick portions of competent, less fractured Mancos Shale. Despite being located only 335 m northeast of PLM7 on the opposite bank of the East River, PLM8 showed no major fracture zones, and shale characteristics were comparable to those observed at GLS1 in terms of visual appearance and fracture density.

AEM data allowed us to assess the electrical properties of the bedrock throughout the watershed. As shown in Fig. 1A, AEM data were acquired along transects from about 0.2 to 17 km in length and in multiple orientations throughout the watershed, with a sounding spacing of ~50 m and a transect spacing of ~200 to 500 m [Fig. 1A; (*35*)]. Because different bedrock units are associated with different characteristic resistivities, here, we focus solely on the regions dominated by Mancos Shale (Fig. 1A). Even within this single unit, the AEM data highlight a distinction between the upper and lower watershed (Fig. 1C). The uppermost 20 m of Mancos Shale of the upper watershed generally shows higher resistivities (258.2 ± 118.2 ohm·m) than the lower watershed (146.4 ± 91.8 ohm·m). In the following,

we will refer to these two separate domains as northern and southern Mancos Shale, based on their location within the watershed, where the northern and southern locations relate to the upper and lower watershed, respectively.

Detailed bedrock characteristics obtained from borehole geophysical measurements

Geophysical borehole logging, including nuclear magnetic resonance (NMR), pore fluid conductivity and temperature, electromagnetic induction, spectral gamma, and flow meter tests, provides high-resolution information on the bedrock properties at each of the borehole locations [Fig. 2; (*57*)]. Groundwater temperatures represent seasonal flow conditions, with the upper part of GLS1 within permeable lacustrine deposits showing colder temperatures and hence increased mixing than observed in the Mancos Shale units of the other boreholes. All boreholes show a characteristic increase in temperature toward the base of the borehole representative of the regional geothermal gradient. Groundwater electrical conductivity (EC) was low in the Mancos Shale of GLS1 and GUM1 (286.6 ± 20.5 and 130.2 ± 25.4 μS/cm, respectively). In contrast, groundwater EC was higher in PLM7 (361.7 ± 8.0 μS/cm) and considerably higher in PLM8 (865.3 ± 11.1 μS/cm). Those values translate to electrical resistivities of the pore fluid of 34.9 to 76.8 ohm·m in the northern and 11.5 to 27.6 ohm·m in the southern Mancos Shale boreholes. Geochemical analysis of groundwater samples taken throughout the watershed corroborated those findings, showing considerable variations in cation and anion concentrations, with elevated chloride, fluoride, and sodium concentrations in the lower part of the watershed (*58*, *59*). This is why we infer that the gradient in pore water electrical properties is partly related to changes in the geochemical environment from the northern to the southern Mancos Shale.

High-resolution measurements of electrical resistivity in the vicinity of each borehole were acquired through in-hole electrical resistivity tomography (ERT), which indicated a range of vertical heterogeneity. Quaternary lacustrine deposits overlying the Mancos Shale in GLS1 show notably lower resistivities (93.1 ± 16.8 ohm·m) than the shale itself, which varies between 485 and 1620 ohm·m, with a mean of 820.4 ohm·m and an SD of 242.3 ohm·m. The lower electrical resistivity values in the shale unit correlate with observed fractures (see lithological description in Fig. 2). At GUM1, resistivities show some variability (350.3 ± 165.1 ohm·m) and generally increase with depth, which agrees with core observations that showed reduced fracturing along the lamination plane at depth. While the Mancos Shale of GLS1 and GUM1 is characterized by resistivities >120 ohm·m, resistivity values recorded within PLM7 and PLM8 are mostly <100 ohm·m. PLM7 generally showed the lowest resistivities (34.7 ± 5.2 ohm·m), with fracture zones being characterized by the lowest observed resistivities. PLM8, despite having no major fracture zones and having visually comparable structural characteristics to the shale recovered from GLS1, showed lower resistivities (76.3 ± 33.8 ohm·m) than recorded in the wells of the northern Mancos Shale. In part, this is attributed to the higher EC of the groundwater recorded in the wells of the southern Mancos Shale. However, a petrophysical analysis of the data showed that the change in fluid EC is not sufficient to explain the observed difference in bedrock resistivity. For the same geological parameters, the change in pore fluid EC from 286 to 865 μS/cm would change the resistivity by about 120 ohm·m, while a difference of about 745 ohm·m was observed. The cause of this difference is interpreted to be a change in the mineral composition, likely due to a higher degree of metamorphism of the Mancos Shale of the northern domain (*60*).

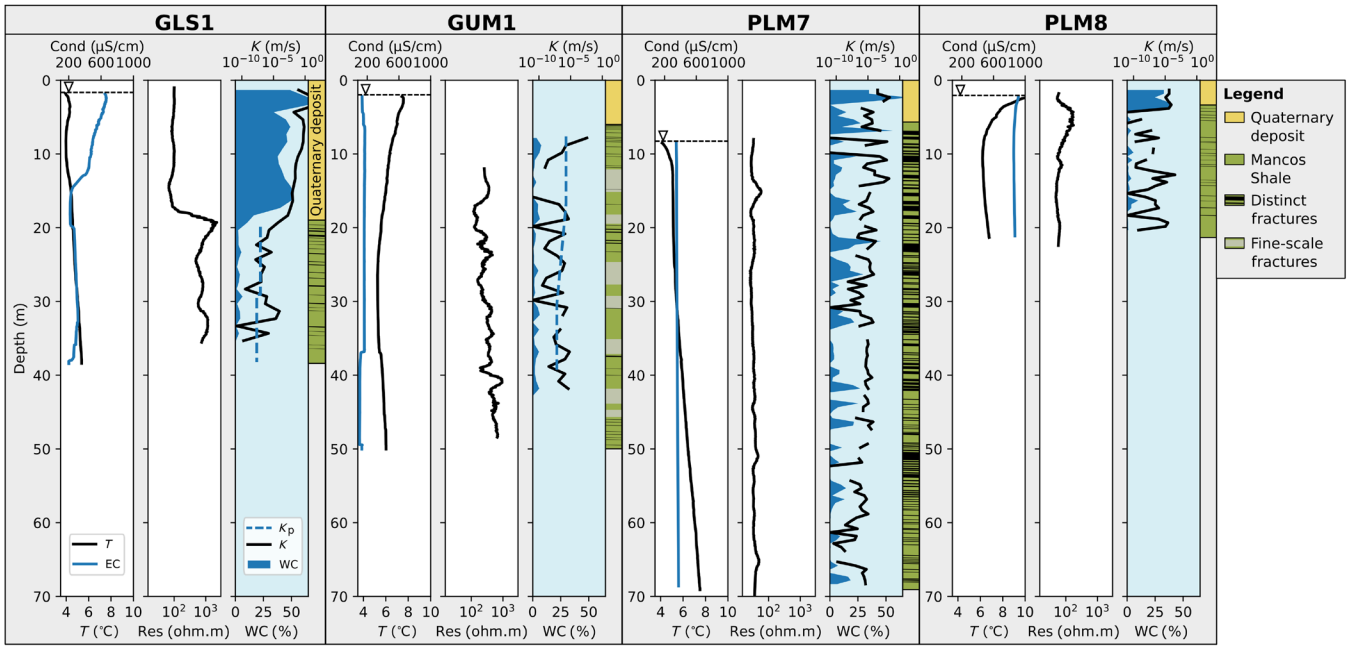

Fig. 2. Bedrock and pore fluid properties obtained from borehole logging. With the exception of GLS1, which had about 20 m of lacustrine deposits overlying the Mancos Shale, boreholes were drilled entirely within Mancos Shale with less than 2 m of soil cover. For each borehole (GLS1, GUM1, PLM7, and PLM8), pore fluid electrical conductivity (EC) and temperature, bedrock electrical resistivity, and bulk water content (WC) and hydraulic conductivity (estimated from NMR measurements) are shown from left to right. Groundwater table as measured during borehole logging is shown with pore fluid temperature and EC. Lithology and locations of major fracture zones are indicated on the right side of each panel and were derived from the drilling notes and core photographs.

Borehole NMR measurements, which are sensitive to the water content and pore size distribution in the vicinity of the borehole, were used to estimate bedrock effective porosity and hydraulic conductivity for depths below the water table (*61*, *62*). Similar to the observations of the borehole fluid conductivity, temperature, and bedrock resistivity, the lacustrine deposits of GLS1 show high effective porosity (45.0%) and hydraulic conductivity (1.0×10^{-1} m/s), while the lower part of the borehole traversing Mancos Shale shows low values (2.9% and 1.42×10^{-7} m/s, respectively). Similar observations are drawn from GUM1, which shows low effective porosity and hydraulic conductivity throughout the borehole (2.8% and 6.9×10^{-8} m/s, respectively). The estimated effective porosity at PLM7 agrees with fracture zones observed in retrieved core and thus is highly variable (8.1 ± 11.6%). Hydraulic conductivities within the Mancos Shale in PLM7 were considerably higher than in the other boreholes (2.1×10^{-6} m/s). PLM8 showed high effective porosity and hydraulic conductivities in the upper 4.5 m below ground level (bgl; 28.5% and 4.2×10^{-6} m/s, respectively), which is composed mostly of weathered rock and hence can be attributed to the weathering zone overlying the unweathered shale. Below this depth, effective porosity and hydraulic conductivity were lower (1.8% and 2.6×10^{-8} m/s, respectively) and comparable with measurements obtained at GLS1 and GUM1.

Petrophysical model using wellbore data to relate electrical resistivity to regolith hydraulic properties

We develop a site-specific petrophysical relationship between the borehole porosity estimates and electrical resistivity and subsequently use this developed relationship to transfer the AEM measurements into regolith hydraulic property estimates. This intrinsically assumes that the resistivity response of borehole and AEM data is comparable (*40*, *63*). Our use of electrical resistivity for this estimation is justified because electrical resistivity is related to the porosity of rocks (*64*). This relationship between electrical resistivity and porosity, however, has been shown to be complex, often site specific (*30*), and dependent on the rock lithology and fluid characteristics. While many studies have shown direct relationships between the resistivity response and hydraulic parameters, most of these studies have considered porous rocks [e.g., (*65*, *66*)]. When dealing with fractured rocks, the relationship becomes more complex, and usually, a dual-porosity concept is used to estimate petrophysical properties (*66*). Generally, an increasing number and width of fractures relate to a decreasing electrical resistivity (*67*, *68*). Relating the resistivity and effective porosity as measured in the boreholes shows that low resistivities generally can be related to high effective porosity (Fig. 3A). Grouping the data in terms of fracture density, with PLM7 having high and PLM8, GLS1, and GUM1 having low fracture density, shows that the high–fracture density group is characterized by high porosity with a large variability, while, for the low–fracture density group, lower porosities with less variability were recorded (2.6 ± 0.9%). For the PLM7 data, it is also worth noting that there is a negative linear correlation between resistivity and porosity (Pearson's $r = -0.64$). The large variability at low resistivities is explained by the fractured nature of the bedrock and the resolution of the ERT measurements, where fracture zones show very high porosity (>20%), while adjacent competent bedrock has very low porosity (<5%), which provides an aggregated response in the ERT data. Similarly, as described above, bedrock resistivity is not only a function of the available pore space but also the mineral composition and pore fluid conductivity. The PLM8 data show the smallest resistivity of the sites, low porosity, and the highest pore fluid EC (Fig. 2). The AEM data show a similar aggregated response, and differences can be associated to the spatial resolution of the data. Although an exponential model could be used to explain the relationship between electrical resistivity and porosity for the entire dataset, the steep rise toward small resistivities would result in poor sensitivity for transforming AEM-derived bedrock resistivities into effective porosity. Hence, we develop an indicator petrophysical model, using 70 ohm·m as a threshold, with values lower than that representing bedrock having higher mean porosity and hence high fracture density, and values above representing bedrock having lower mean porosity and low fracture density.

An inverse relationship between resistivity and hydraulic conductivity can be observed, with lower bedrock resistivities showing higher hydraulic conductivities (Fig. 3B). The effective porosity of fractured rocks is known to often be directly proportional to hydraulic conductivity (*69*). A linear trend (Pearson's $r = 0.59$) is observed for the log-transformed variables with increasing porosity

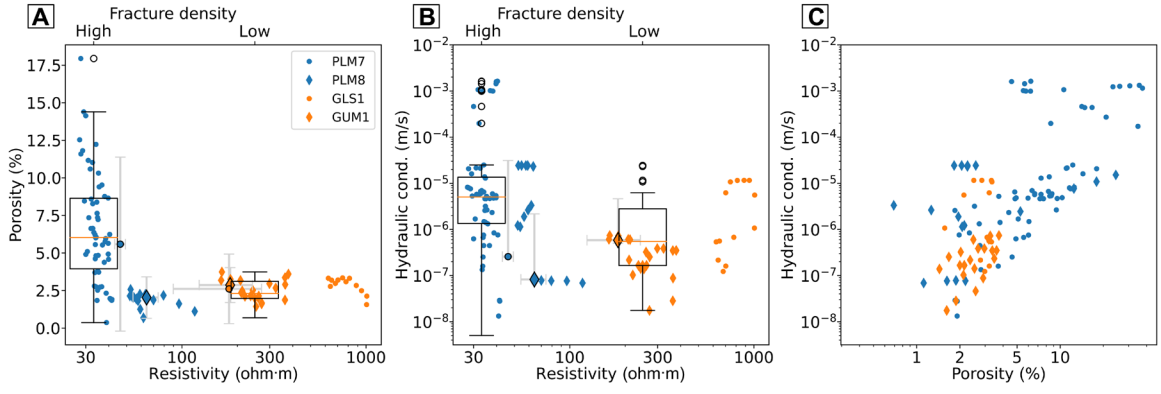

Fig. 3. Petrophysical relationships linking bedrock electrical resistivity with porosity and hydraulic conductivity. Relationship between electrical resistivity and porosity (**A**) established from the in-hole ERT and NMR measurements. Boxplots are shown for data of high (PLM7) and low fracture density (GLS1, GUM1, and PLM8). (**B**) Relationship between electrical resistivity and hydraulic conductivity and boxplots of the data grouped on the basis of fracture density. (**C**) Linear relationship between log-transformed porosity and hydraulic conductivity (Pearson's $r = 0.59$). Symbols are outlined in black, and gray error bars indicate the averaged AEM-related subsurface response.

showing increasing hydraulic conductivities (Fig. 3C). Hence, for the investigated Mancos Shale, low resistivity can be associated with having high porosity, hydraulic conductivity, and fracture density.

Determining geomorphic indices and vegetation types

Geomorphic indices were derived from high-resolution airborne LiDAR data, which were acquired in August 2015, using a Riegl Q1560 dual-channel LiDAR system (*70*). The point density exceeds 8 pulse/m^2. From the LiDAR point cloud, a digital terrain model (DTM) was computed, representing the bare ground at a spatial resolution of 0.5 m. The DTM was compared to real-time kinematic GPS measurements, showing root mean square errors of less than 0.15 m (*70*). Using Landlab (*71*), we calculated the slope and aspect from a DTM that was smoothed and reduced in resolution to 5 m. The elevation ranges from 2700 to 3400 m, and slopes have a mean angle of 25.5°, with a maximum of 68.1°. Slopes are mostly oriented along two main directions, northeast and southwest.

Vegetation distribution was derived from WorldView-2 satellite imagery, acquired in September 2015. WorldView-2 provides panchromatic images of 0.5-m resolution and multispectral imagery of eight bands including the visible and near-infrared ranges at spatial resolution of 2 m. Using pan sharpening, the multispectral image resolution was improved to 0.5 m (*70*). A supervised machine learning approach was used to estimate the plant community distribution, based on an extensive ground-truth dataset. The classification methodology is detailed in (*70*). The identified vegetation types were grouped into five classes: meadow plants, shrubs, deciduous and evergreen forests, and barren land. These classes account for 57.8, 8.3, 15.3, 10.9, and 7.7% of ground cover, respectively.

Estimating regolith properties across the watershed and spatial variability of the influence of bedrock on geomorphic and vegetation properties

The inverted AEM data reveal differences between the lower and upper watersheds (Fig. 4), with the lower watershed generally showing lower resistivities. With higher resistivities (>500 ohm·m) than the surrounding Mancos Shale, the data also indicate the granodiorite laccoliths of Mt. Snodgrass, Mt. Gothic, and Mt. Crested Butte. Similarly, known outcrops of the granodiorite Copper Creek sill are related to resistivities >500 ohm·m east of GUM1. Beyond the variability within the Mancos Shale, the resistivity generally agrees with the geologic map, both spatially and along transects (Fig. 5). This suggests that subsurface electrical properties are a good proxy for distinguishing different geological units and characterizing heterogeneity within units such as the Mancos Shale. We also qualitatively compared the AEM-derived subsurface electrical resistivities with data acquired on the surface and in the boreholes (Fig. 6). Although the surface and borehole data provide more detail than the AEM data, the datasets show comparable amplitude and feature distribution and are generally in agreement.

After establishing a relationship between borehole geophysical and regolith hydraulic properties, we test the hypothesis that geomorphic indices and vegetation type can be used to describe the bedrock electrical and hydraulic properties on a watershed scale. We explore relationships between the AEM-inverted shallow subsurface resistivity (i.e., the mean resistivity of the upper 20 m bgl) of the Mancos Shale–dominated units, and geomorphic indices (elevation, slope, and aspect), and vegetation type (Figs. 7A and 8; (*72*)]. Given the local geology, the upper 20 m is generally representative of the subsurface response of the soil and weathered bedrock. The data show significant linear relationships between resistivity and the geomorphological indices, with increasing resistivity for increasing elevation and slope (Pearson's $r = 0.38$ and 0.13, respectively, and $P << 0.01$). Higher elevations tend to have steeper slopes, which are mostly southeast (SE) or northwest facing. While resistivity and elevation show distinct distributions for the southern and northern Mancos Shale, slope and aspect have comparable distributions for both areas, although the northern Mancos Shale domain shows a higher portion of SE-facing slopes compared to the southern Mancos Shale domain. Vegetation type shows covariability with subsurface

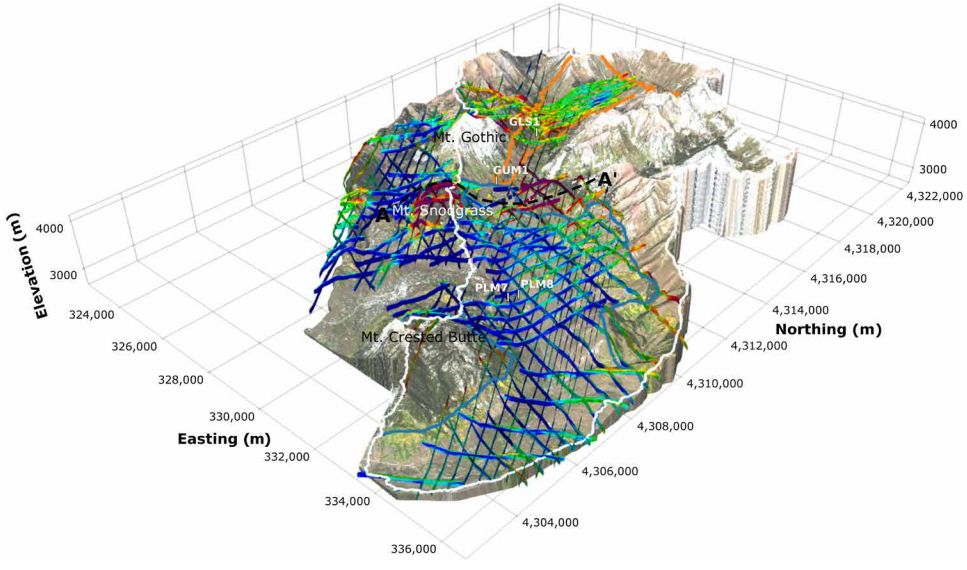

Fig. 4. AEM data covering the East River watershed. The figure shows the upper 100 m of each inverted flight line, placed above the surface topography. Topographic data are based on LiDAR data and colored using WorldView-2 data (*72*). Gaps in the AEM data are due to restrictions in access and air space. Shown also are the borehole locations and the outline of the cross section (dashed black line) shown in Fig. 5.

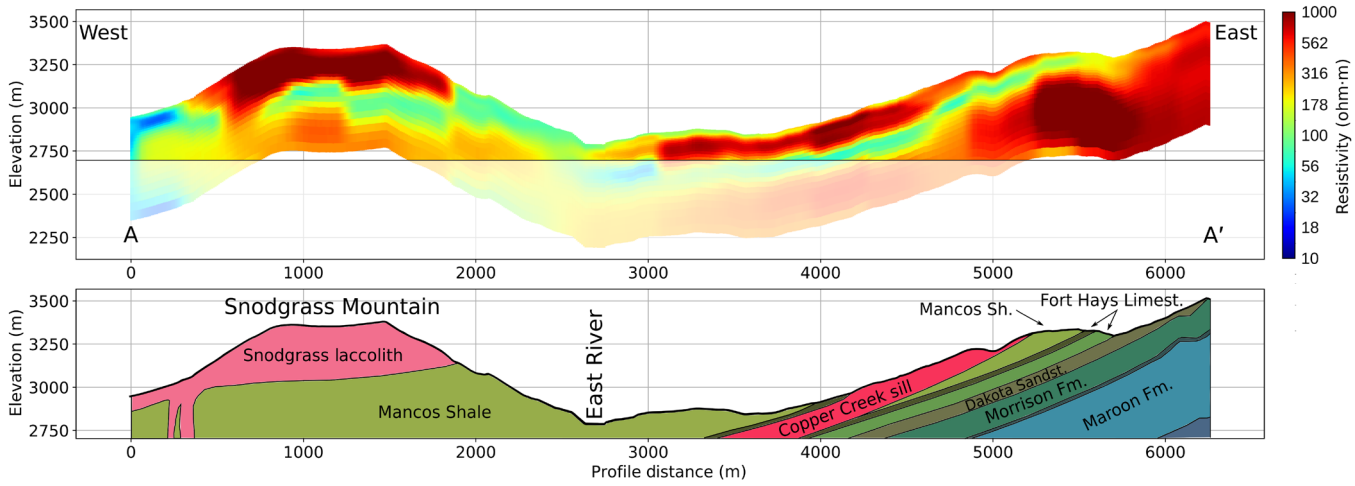

Fig. 5. Comparison between AEM-derived subsurface resistivity distribution and geological cross section. Figure 4 shows the location of the cross section, which spans from west of Mt. Snodgrass to the eastern end of the watershed. The geological cross section was modified from (*44*). Note that the blended area in the top panel indicates the area that is not shown by the geological cross section.

resistivity (Fig. 8), where shrub- and meadow-covered areas are characterized by lower resistivities than those covered by forests. Within forests, deciduous tree types are related to lower-resistivity bedrock than conifers. The differences in these distributions are statistically significant. Exploiting those relationships, we train a machine learning method, called extremely randomized trees regression (ERTr) model (*73*), to estimate shallow subsurface resistivities for each Mancos Shale domain. The data estimated using the regression models fit the measured data well (R^2 = 0.64; Fig. 7B). Training a single model without considering the two domains separately failed, as the data fit, in particular for the northern Mancos Shale, deteriorated. The three geomorphological indices are of most importance to the ERTr model, with elevation, aspect, and slope having a relative feature importance of 0.29, 0.27, and 0.24, respectively, and the vegetation having a relative importance of 0.07. Our results indicate a strong correlation between the surface topography, geomorphology, and bedrock properties.

Using the ERTr model, we predict the shallow resistivity across the watershed from remotely sensed geomorphic indices and vegetation-type estimates (Fig. 9) and make use of the relationships developed from the borehole data to transform the resistivity to an estimate of fracture density. We used this intermediate step to overcome the small number of borehole observations, which prevented us from directly linking the surface metrics to the fracture density. We limited the analysis to areas characterized by the Mancos Shale because the model was trained on data from this bedrock type only. Within the northern Mancos Shale, estimated resistivities are comparably high (265.9 ± 78.7 ohm·m), while the southern Mancos Shale shows considerably lower resistivities (136.3 ± 60.8 ohm·m). The spatial variability of estimated fracture density shows distinct spatially connected fracture zones. In particular, the anomaly that characterizes PLM7 could possibly be associated with a mapped fracture zone to the south of it (*44*). While the southern Mancos Shale shows numerous linear features having low resistivity that are interpreted as fracture zones, the northern Mancos Shale shows resistive linear features in its southwestern part that relate to granodiorite outcrops on the eastern flank of Mt. Gothic. No fracture zones that could be related to areas of increased effective porosity are evident from the data within the northern Mancos Shale.

Previous approaches using geomorphic indices assumed a constant relationship between regolith thickness and geomorphic indices across a site [e.g., (*19*)]. To investigate the stationarity of the developed relationship, we calculated the model misfit and the SD of the governing topographic and vegetation metrics across the watershed (Fig. 10). We focused our analysis on 10 subcatchments, which were defined using a DTM with 1-m cell size, and as before limited our analysis on the part of the watersheds that are characterized by Mancos Shale. The relative root mean square error calculated on the basis of the observed and predicted resistivity values within each subcatchment varies between 5 and 12%. The smallest errors are in the northernmost part of the study area, and the highest errors are in the eastern part. Linking the errors to the SD of the input parameters, we observe that, generally, lower variability in the input parameters results in smaller prediction errors. That indicates that the prediction is more accurate in smaller regions, where topographic metrics and vegetation distributions can more safely be considered to be stationary compared to larger regions that have more variability.

DISCUSSION

Our analysis provides the first study to test the covariability of above- and belowground features on a watershed scale. We correlate shallow subsurface resistivity (<20 m bgl), which is a proxy for shallow bedrock properties, with topographic indices and vegetation cover and show that a linear correlation exists between the subsurface and surface properties. Other studies have developed similar relationships to link or predict subsurface properties from surface geomorphological observations, but their analysis was based on a small number of subsurface observations (*74*, *75*). The correlation between bedrock and vegetation distribution and productivity is shown by other studies and is linked to variations in water-holding capacity, fracture density, and nutrient supply (*76*–*78*). We show that steeper slopes generally relate to higher bedrock resistivity, which can be linked to a higher rock strength (*79*). This is explained by either a smaller effective porosity or fracture density, reduced water saturation of the rocks forming these slopes, or a combination. This

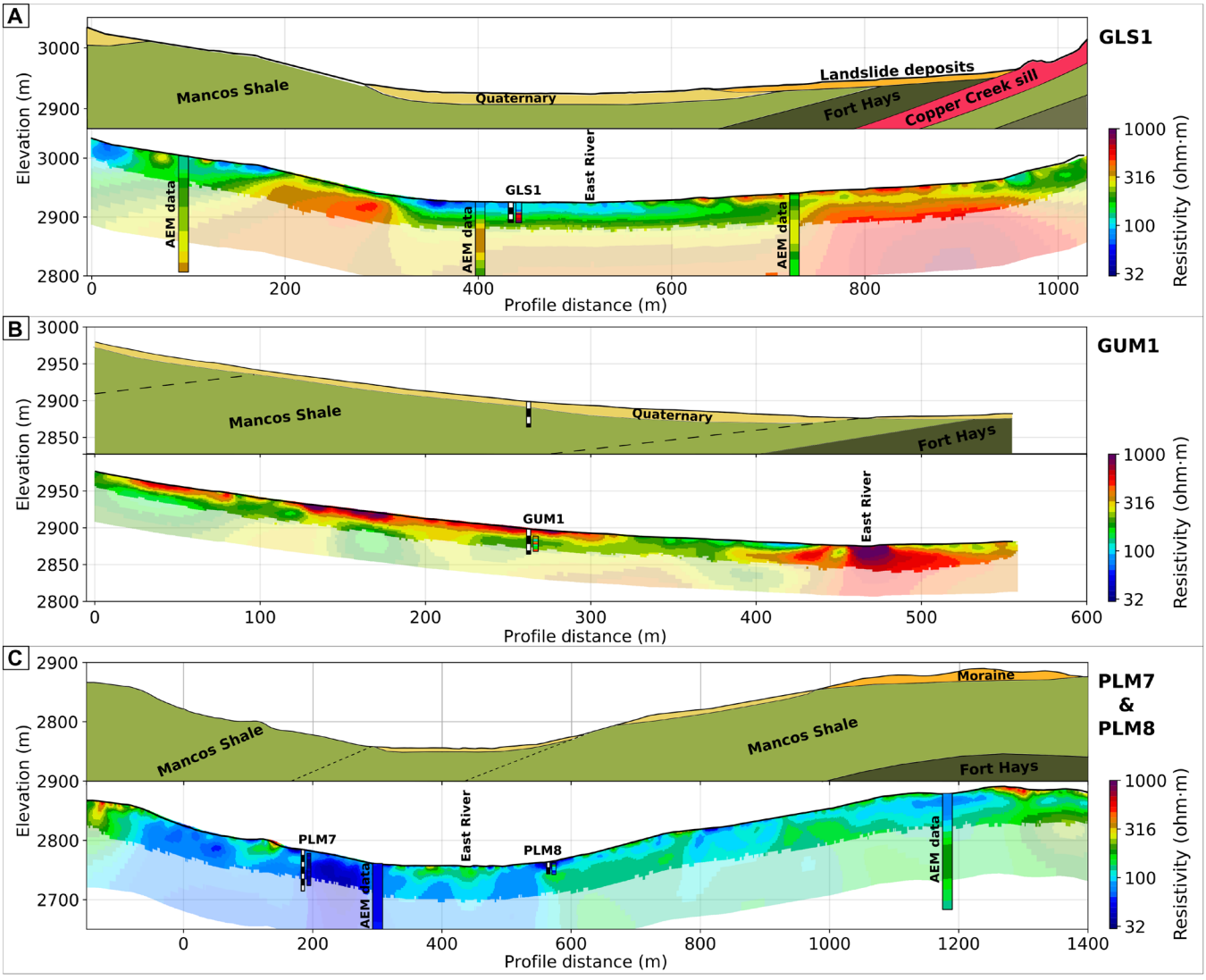

Fig. 6. Site geological and geophysical cross sections showing agreement between geologic map and subsurface resistivities. Shown are data of the upper watershed (**A**, **B**), and of the lower watershed (**C**). For GLS1 (A), and PLM7 and PLM8 (C) AEM data points are shown, highlighting the agreement between surface ERT and AEM data. For each borehole location, the results of in-hole ERT measurements are shown, which are also in agreement with the surface data. This highlights that subsurface resistivities are a suitable proxy for estimating subsurface conditions within the East River watershed. The geological cross sections were drawn on the basis of the geologic map (*44*).

is in agreement with other studies that showed that steeper slopes are usually related to higher runoff and less groundwater infiltration [e.g., (*23*)], while increased soil erosion leads to a thinner soil cover (*80*), which also likely contributes to a higher aggregated resistivity response.

By relating the subsurface with surface observations in an ERTr model, more than 64% of the data variability is explained. A multidimensional relationship between surface parameters and subsurface properties indicates that (i) increases in slope and elevation are related to increases in resistivity and (ii) forests generally grow on higher-resistivity bedrock than meadows and shrubs do. Of the variability not explained by those parameters (36%), most are likely related to inherent bedrock properties (such as grade of metamorphism, mineralization, deep fractures, and faulting), and changing hydrogeochemical conditions that alter weathering rates and subsurface flow conditions (*60*, *81*). This indicates that geomorphological models based on such relationships are able to recover general trends of subsurface conditions, but that they may fail in addressing the full heterogeneity, especially in cases of stratigraphically and tectonically complex geological conditions. Although those models provide a reasonable estimate, direct and geophysical observations are required to build a subsurface model that is representative of the local and regional subsurface conditions, and AEM data can be a valuable dataset to fill this lack of multiscale subsurface imaging. This approach, which combines multiscale measurements, presents an opportunity to investigate shallow bedrock properties in unprecedented detail across a watershed. It will allow us to parameterize hydrological models to study the impact of disturbances on mountainous watersheds and will aid in focusing future research efforts to target specific bedrock features identified from this high-resolution dataset. Our

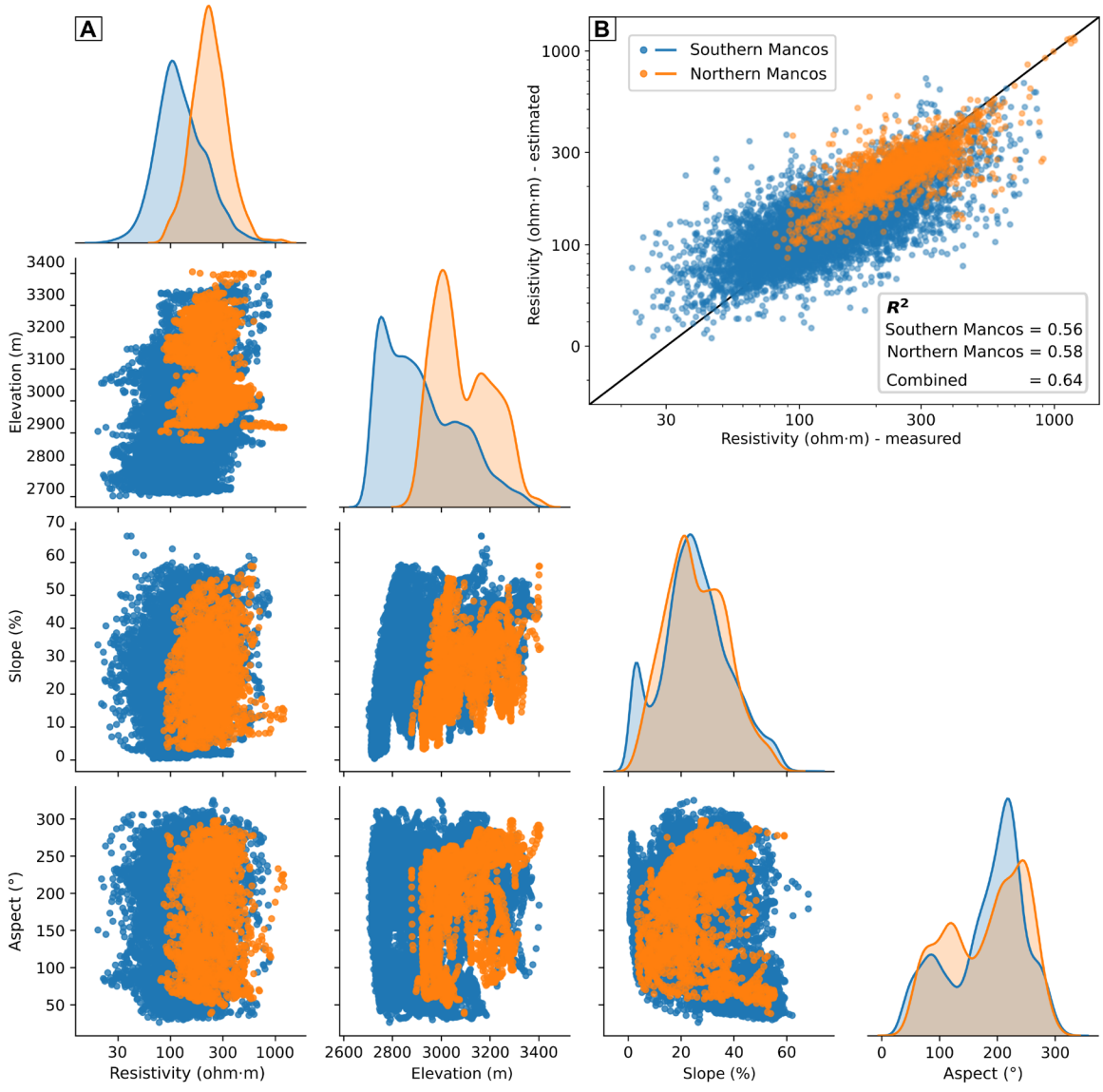

Fig. 7. Relationships between subsurface electrical resistivity and geomorphological indices. We analyzed 13,524 data points of colocated AEM-derived averaged shallow resistivity, slope, aspect, and vegetation types. (**A**) Cross-plots and distributions of mean subsurface electrical resistivity (<20 m bgl), elevation, topographic slope, and incoming shortwave radiation at AEM locations within the northern and southern Mancos Shale, as defined in Fig. 1. (**B**) Cross-plot of measured and estimated electrical resistivity. Estimation based on random forest regression using elevation, slope, radiation, and vegetation type (*72*) as estimators. The random forest regression model explains 64% of the data variance.

approach could be extended by including geochemical and hydrological measurements and linking those to various surface features to estimate the spatial variability of these measurements [e.g., (*82*)]. However, such applications would also require a covariability between surface and hydrobiogeochemical features, which has yet to be shown.

Although the East River watershed is known to be dominated by a single bedrock unit, Mancos Shale, we show that bedrock hydraulic properties vary systematically within this unit. While the northern Mancos Shale is characterized as a mostly unfractured shale with low effective porosity and low hydraulic conductivity, the southern Mancos Shale shows notable variability in those properties. These are controlled by deep faults and fracture zones that show high porosity and hydraulic conductivity, while outside those zones, porosity and hydraulic conductivity are low. The binary classification map of fracture density (Fig. 9B) relates many linear features in the southern Mancos Shale to extensive fracture zones, which were not evident in the northern Mancos Shale. From the ground-based ERT data (Fig. 6), a Popper-Bayes hypothesis testing method has recently been used to determine the geological origin of a low-resistivity anomaly at PLM7 (*83*). Their results show this anomaly to be representative of a normal or high-angle reverse fault, or a potential sackung feature, which is located along one of those linear features (Fig. 9C). Fault and fracture zones are interpreted to not have a surface expression (such as at PLM7) but likely impose major control on hydrological processes, such as strong anisotropic flow (*25*). Hence,

modeling approaches that neglect the fracture control will not fully capture watershed behavior as it pertains to preferential fluid flow and transport. Similarly, Mancos Shale is a thick formation [up to 1500 m; (*48*)], which shows lateral and vertical heterogeneities in hydrological properties due to alternating depositional environments that range from shallow to deep water. Although not discussed in detail here, hydrological conditions are expected to vary considerably between different bedrock types, e.g., the granodiorite of the laccolithic intrusions potentially outweighing the intra–Mancos Shale variability.

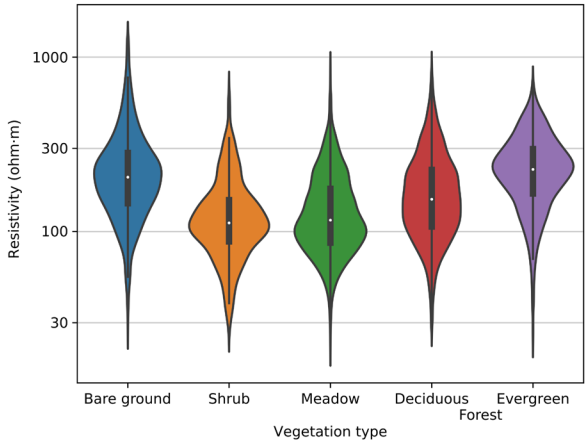

Fig. 8. Distribution of Mancos Shale shallow resistivity (<20 m bgl) for different vegetation types. Analyzed resistivity is the mean of the upper 20 m bgl; vegetation types were derived from hyperspectral data (*72*).

Despite the linear features that are related to fracture zones, the southern Mancos Shale generally shows lower resistivities than the northern domain, which is associated to a change in grade of metamorphism and pore fluid conductivity but could also be associated with changes in the depositional regime of the Mancos Shale. Because the pore fluid conductivity is directly linked to the bulk resistivity response of the subsurface, we investigated the potential impact of this parameter on our results. However, changes in pore fluid conductivity cannot solely explain the observed resistivity differences between the upper and the lower watershed. Rock sample analysis indicates a general trend of increasing shale metamorphosis toward higher elevations of the watershed, changing the mineralogical composition (*60*), due to proximity to intrusive rocks and hence changes in hydrothermal conditions (*81*). Higher grades of metamorphism are assumed to relate to a higher resistivity. The location where the AEM data map the change agrees with previous results that indicate shale induration at a similar location (*81*). The observed gradient in pore fluid conductivity of the boreholes likely represents different geochemical environments within the watershed including those that span adjacent hillslopes. These differences in hydrological and geochemical conditions are interpreted to affect seasonal variations in concentration-discharge relationships as different landscape components become hydrologically activated at different times of the water year (*84*).

The scale and resolution of geophysical measurements are critical in studying the heterogeneity of watersheds. While borehole and surface geophysical techniques provide high-resolution data (centimeters

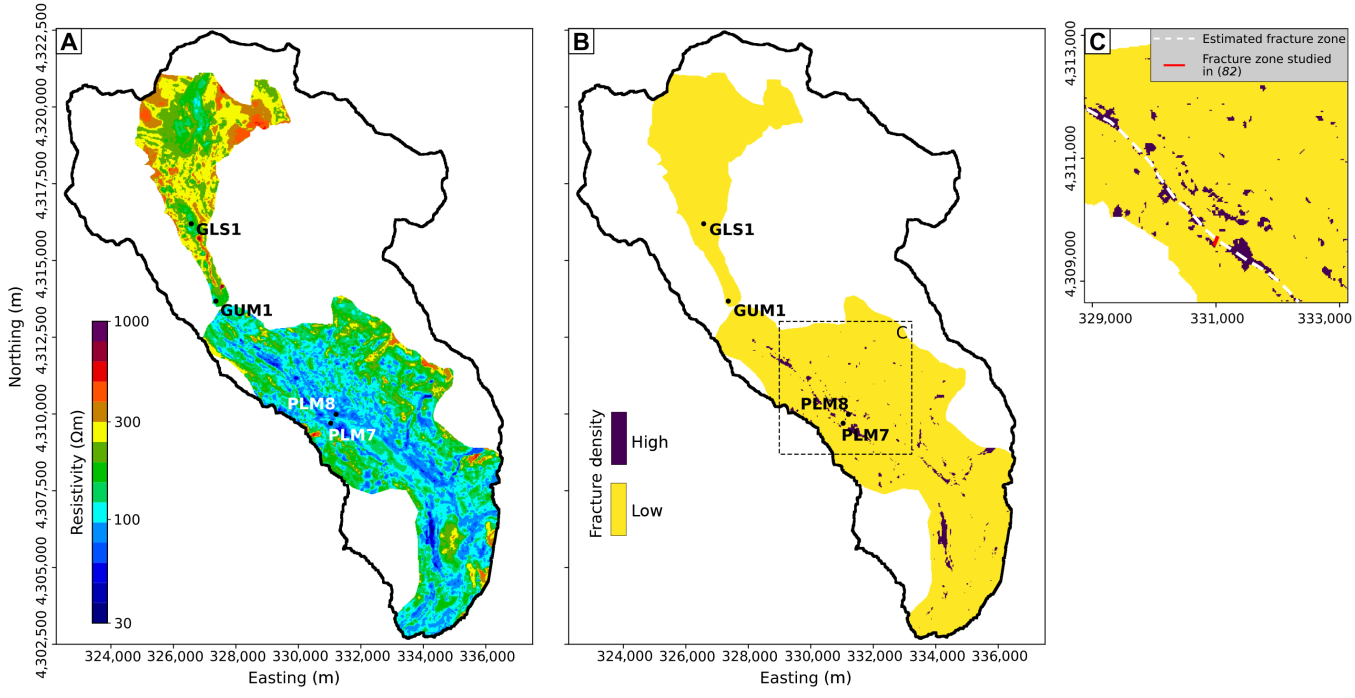

Fig. 9. Predicted shallow subsurface resistivity and fracture density. (**A**) Resistivity is predicted using an ERTr (*73*) model, using topographic elevation, slope, aspect, and vegetation type as estimators. The variation in resistivity (low resistivity in the lower watershed, high resistivity in the upper watershed) agrees with observational studies (*60*) showing a higher degree of metamorphism in the upper watershed. (**B**) Fracture density is defined on the basis of the relationship gained from the borehole data using a resistivity of 70 ohm·m. Linear features showing areas of high fracture density are postulated to correspond to fracture zones. (**C**) The area of the fracture zone analyzed in (*83*) lies along the estimated and known fracture zones.

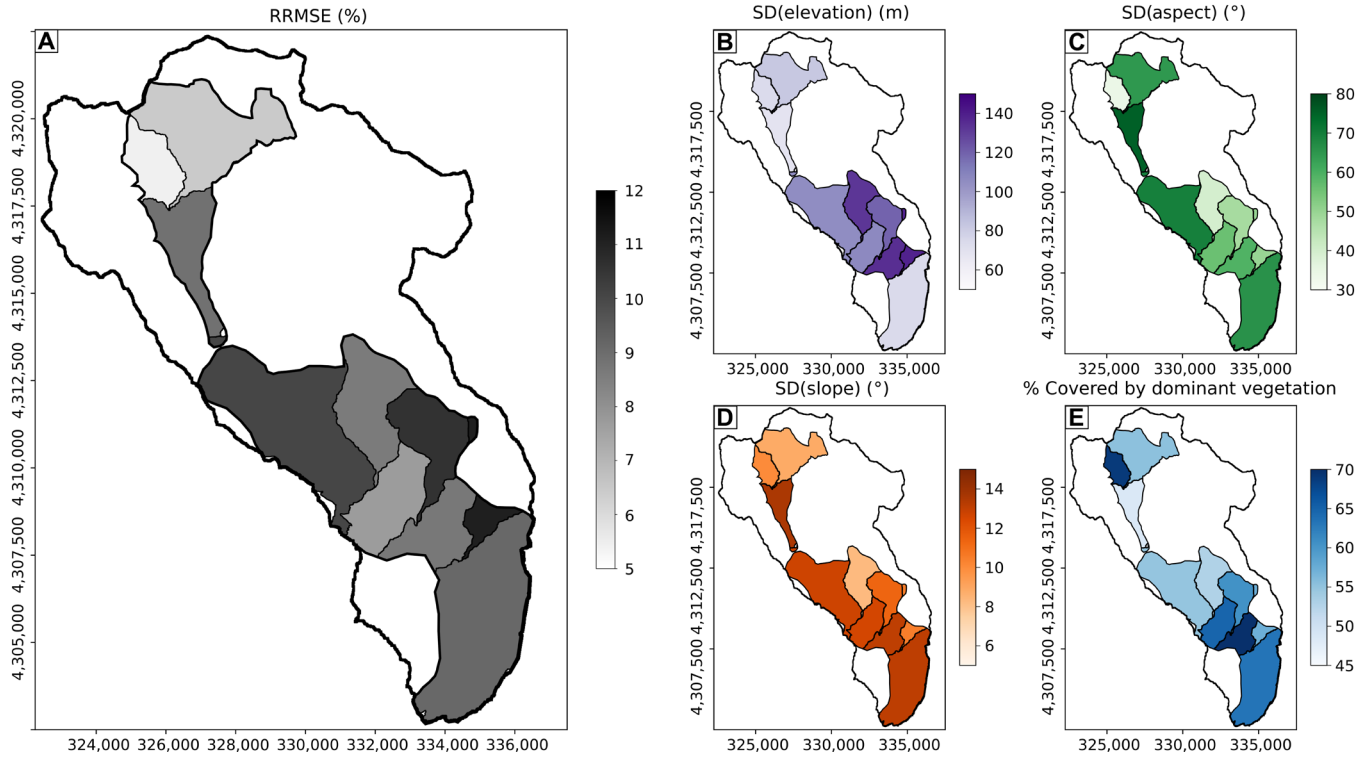

Fig. 10. Spatial variability of prediction accuracy. (**A**) Relative root mean square error (RRMSE) of the predicted resistivity values for several sub-basins within the Mancos Shale–dominated part of the East River watershed. Variability of the prediction inputs plotted against (**B**) elevation, (**C**) slope aspect and (**D**) angle, and (**E**) percentage of the basin covered by the dominant vegetation type.

to meters), these measurements are usually restricted to the hillslope scale, and hence, sampling of watershed heterogeneity at scales more directly relevant to water managers is almost impossible. AEM measurements complement these techniques to provide bedrock resistivity at the watershed scale at a resolution that is adequate to study larger-scale bedrock variability and faults. To bridge the resolution, we only consider an aggregated response for the AEM measurements and define a dimensionless bulk measure, high or low fracture density, to interpret the estimated shallow bedrock resistivity, while we define the electrical response of the bedrock column in detail at borehole locations. By using this aggregated response and considering the sensitivity of the airborne measurements, we assume that most of the response originates from the shallow bedrock and in the saturated zone. Because surface deposits are thin throughout the watershed and water tables usually close to the surface (<10 m bgl), this assumption is valid but could be violated at other research sites. In addition, this study focuses primarily on a single unit, the Mancos Shale, to better isolate the relationship between resistivity and fracture density, which may be more complex when considering multiple geologic units. Although we show that AEM and borehole and surface geophysical data provide comparable responses at our study site, this may not be generally the case. Because the measurement principles are different, the subsurface response may be different too. The quantitative comparison between borehole, surface, and airborne geophysical methods therefore requires still more research.

In conclusion, we show that variations in geomorphic properties and vegetation types correlate with bedrock properties and that these bedrock properties vary considerably throughout a single geological unit, the Mancos Shale. This change is governed by variations in fracture density and pore water conductivity, which affect subsurface flow and transport processes. We postulate that the tectonic history, including the laccolith intrusions, changed the Mancos Shale mineralogical composition and created a complex fracture network in the East River watershed, which are both expressed in the electrical resistivity of the bedrock. Those heterogeneities, in turn, control geomorphological processes, such as soil production and erosion, and the ecohydrological parameter distributions, which are ultimately expressed in vegetation distribution. Hence, models aiming to assess the impact of disturbances on groundwater flow and transport dynamics should incorporate these heterogeneities to address the complexity of subsurface processes, as these affect current and future concentration-discharge relationships (*3*). This feedback, however, is complex and more work is required to understand the coevolution of subsurface features and geomorphological and vegetation dynamics.

A thorough multiscale subsurface characterization of a watershed from plot to regional scale enables detailed understanding and modeling of subsurface flow and transport to assess and predict the impact of disturbances onto a complex hydrological system. While we show this applied to the mountainous East River watershed, similar observations are expected from headwater to coastal systems, where bedrock properties are critical for groundwater research and management. The results of our study support the validity of geomorphological models that use surface expressions to estimate bedrock properties yet highlight some of the limitations of these models.

We also showed that these relationships are not stationary, with areas of less variability in surface metrics related to smaller model misfits. We envision that the geomorphology and vegetation distribution can be used to scale the subsurface properties from the geophysical data locations to a larger scale, as well as to guide subsurface characterization in such a way to identify the key regions for quantifying the subsurface-surface covariability.

MATERIALS AND METHODS

Experimental design

Our analysis builds upon drilling data, near-surface and airborne geophysical data, and remote sensing data acquired within the East River watershed (*35*, *57*, *72*). These techniques were chosen not only to characterize bedrock properties in detail but also to provide data representing the variability of subsurface conditions throughout the watershed. The watershed contains designated areas of wilderness and private land that were not accessible; hence, data acquisition was restricted to locations within a permit provided by the U.S. Forest Service. AEM data were acquired in 2017 (*35*), and on the basis of those results, which show large-scale variations in bedrock properties, borehole locations and accompanying surface geophysical surveys were placed. Those locations provide detailed information on bedrock properties representative of different bedrock features identified from the AEM data. Within previous studies, detailed topographic data were collected using airborne LiDAR measurements, and vegetation has been classified using hyperspectral data (*70*, *72*). Both datasets were used in this study and provided data across the entire watershed at 0.5-m resolution.

Borehole drilling and geophysical logging

Boreholes were drilled using rotary drilling, with core recovery throughout the Mancos Shale. With the exception of GLS1, which could be logged with an open hole, borehole stability required immediate installation of polyvinyl chloride casing; hence, geophysical logging was performed in the cased borehole. This limited the number of geophysical parameters that could be measured. Along with fluid temperature and conductivity (Fig. 2), we acquired electromagnetic induction, spectral gamma, and heat pulse and spinner flow data using Mount Sopris QL-40 borehole tools (Mount Sopris Instruments, Denver, CO). Borehole nuclear magnetic data were recorded at 1-m intervals using a Vista Clara Javelin system [Vista Clara Inc., Mukilteo, WA; (*85*)]. The raw data were inverted for T_2 relaxation time distribution (*62*), which, in turn, was used to calculate depth-resolved total porosity and permeability (*86*). The permeability was calculated on the basis of the Schlumberger-Doll-Research model (SDR) and transformed into hydraulic conductivity following (*87*)

$$K = k(\rho g/\mu)$$

with the gravity g, density ρ, and dynamic viscosity μ of water. The parameters of the SDR model, i.e., the formation-dependent variable C, were calibrated using constant head step tests (*88*), performed in GLS1 and GUM1, by minimizing the difference between the measured and estimated hydraulic conductivities. Recovered cores were examined and photographed and are archived at the U.S. Geological Survey core repository in Denver, Colorado (*56*). The core observations were used to identify fractures at each borehole location (Figs. 1 and 2) and to derive an estimate of the fracture density.

Near-surface and borehole geophysical imaging

ERT data were acquired along the surface and within the boreholes using an AGI SuperSting R8 system (AGIUSA, Austin, TX) to obtain high-resolution images of the subsurface electrical resistivity distribution. At the surface, data were acquired using 112 electrodes at 5-m spacing and using a dipole-dipole acquisition scheme, with dipole lengths a of 5, 10, 15, 20, 25, 30, 35, and 40 m. For the borehole measurements, 56 electrodes at 0.6-m spacing were used, using a dipole-dipole array with dipole lengths a of 0.6, 1.2, 1.8, 2.4, and 3.0 m. For both, dipole separations of 1 to 8a were used. The data were inverted using a finite element, fully parallelized inversion code [E4D, (*89*)], using an L2 norm for the model misfit. The final misfit for the surface data ranged from 2.1 to 3.1% and from 1.6 to 3.9% for the borehole data. To represent the resistivity variation around the borehole, we extracted the resistivities between a distance of 0.5 and 1.0 m from the center of the borehole and averaged those values at 0.5-m intervals along the depth of the borehole. The data were then used to calculate the petrophysical relationships (Fig. 3). To account for the different resolution of borehole NMR and ERT, we applied a Gaussian filter with a characteristic length of 1 m to both datasets.

AEM imaging

AEM data were acquired using a helicopter-mounted VTEM-ET system, which has a 17.4-m diameter transmitter loop with two turns. To create a primary electromagnetic field, a current of 230 A was introduced in this loop and turned off rapidly within 500 μs. This primary field then introduces eddy currents within the subsurface, which create a secondary electromagnetic field that is sampled by the receiver coil from 5.2 μs to 8.8 ms after the current turnoff. Given topographic and access restrictions, AEM flight paths were designed to allow for dense sampling of subsurface properties. AEM data were manually edited to remove the influence of noise from man-made structures such as powerlines or nearby buildings, and soundings were averaged into regular 1-s output intervals (roughly 50-m spacing along flight lines). Deterministic inversions of the processed AEM data were performed using the AarhusINV code (*90*) implemented in the Aarhus Workbench software (v. 6.3.0.0, Aarhus Geosoftware, Aarhus, Denmark). A smooth, laterally constrained, 30-layer model was used with layer-top depths ranging between 4 and 800 m and layer thickness increasing with depth (*35*). The maximum phase angle parameterization (*91*) was used to estimate electrical resistivity values for each layer, along with additional parameters needed to fit induced polarization effects observed in portions of the data. An estimated depth of investigation (DOI) for each sounding location was calculated (*92*) and indicates the depth to which data constrain parameter estimates. Before further analysis, soundings with poor convergence of the inversion ($\chi^2 > 1.5$), resistivities deeper than the DOI, and values <5 ohm·m were removed from the dataset.

Statistical analysis

For the analysis of subsurface resistivity with regard to topographic and vegetation indices, we first averaged the data of the upper 20 m and transformed it into log space. This depth was defined on the basis of the characteristics of the AEM acquisition system but also

assumed to be a reasonable depth to which bedrock properties affect surface conditions. To do the regression analysis, the slope and aspect were estimated from the LiDAR-derived digital elevation model using Landlab (*71*). Elevation, slope, and aspect were averaged, and the most abundant vegetation type was calculated across a 100-m radius around each AEM sounding point located within areas characterized by Mancos Shale (Fig. 1). For this analysis, we tested radii between 10 and 250 m. While correlation between these parameters and the resistivity increased significantly from 10 to 100 m, at radii above 100 m, correlation increased only slightly. Hence, we chose 100 m as the length scale for our analysis, which is also comparable to the shallow footprint of the AEM system. The ERTr model (*73*) was trained on the scaled data of the southern and northern Mancos Shale, using the scikit-learn package for machine learning in Python (*93*). From the 13,524 data points, 10,819 were used to train the model and 2705 for validation. The model was then applied to a 20 m by 20 m grid covering the northern and southern Mancos Shale domains. Equal to the training data, for each grid cell, elevation, slope, and aspect were averaged, and most abundant vegetation type was estimated for a radius of 100 m, before applying the regression model. Using a threshold of 70 ohm·m, the inverted resistivities were transformed into areas of low and high fracture density.

A single regression model could not explain the measured data to an acceptable level. Instead, we had to include the subdomain as a feature, which emphasizes the control of bedrock geology and properties on subsurface resistivity. This also shows that, while the approach is transferable, the model and relationships may not be applicable to a different watershed or even a different domain (e.g., characterized by a different bedrock type) within the same watershed. We applied a similar analysis to smaller domains and found increasing correlation between surface and subsurface variables with decreasing domain size. We attribute this behavior to the increasing complexity of domains covering wider areas. Simple relationships may be able explain subsurface properties on a small scale [e.g., (*70*)], but the same relationships may have limited applicability to a different or wider domain. Nevertheless, this study provides further evidence that surface topographic features are controlled by subsurface properties and that geomorphological models can provide first-order estimates of subsurface properties, while geophysical studies can provide detailed subsurface information.

REFERENCES AND NOTES

1. Y. Fan, M. Clark, D. M. Lawrence, S. Swenson, L. E. Band, S. L. Brantley, P. D. Brooks, W. E. Dietrich, A. Flores, G. Grant, J. W. Kirchner, D. S. Mackay, J. J. McDonnell, P. C. D. Milly, P. L. Sullivan, C. Tague, H. Ajami, N. Chaney, A. Hartmann, P. Hazenberg, J. McNamara, J. Pelletier, J. Perket, E. Rouholahnejad-Freund, T. Wagener, X. Zeng, E. Beighley, J. Buzan, M. Huang, B. Livneh, B. P. Mohanty, B. Nijssen, M. Safeeq, C. Shen, W. Verseveld, J. Volk, D. Yamazaki, Hillslope hydrology in global change research and earth System Modeling. *Water Resour. Res.* **55**, 1737–1772 (2019).
2. J. P. Field, D. D. Breshears, D. J. Law, J. C. Villegas, L. Lopez-Hoffman, P. D. Brooks, J. Chorover, G. A. Barron-Gafford, R. E. Gallery, M. E. Litvak, R. A. Lybrand, J. C. McIntosh, T. Meixner, G. Y. Niu, S. A. Papuga, J. D. Pelletier, C. R. Rasmussen, P. A. Troch, Critical zone services: Expanding context, constraints, and currency beyond ecosystem services. *Vadose Zone J.* **14**, vzj2014.10.0142 (2015).
3. L. E. Condon, K. H. Markovich, C. A. Kelleher, J. J. McDonnell, G. Ferguson, J. C. McIntosh, Where is the bottom of a watershed? *Water Resour. Res.* **56**, e2019WR026010 (2020).
4. C. Rasmussen, P. A. Troch, J. Chorover, P. Brooks, J. Pelletier, T. E. Huxman, An open system framework for integrating critical zone structure and function. *Biogeochemistry* **102**, 15–29 (2011).
5. E. F. Wood, J. K. Roundy, T. J. Troy, L. P. H. van Beek, M. F. P. Bierkens, E. Blyth, A. de Roo, P. Döll, M. Ek, J. Famiglietti, D. Gochis, N. van de Giesen, P. Houser, P. R. Jaffé, S. Kollet, B. Lehner, D. P. Lettenmaier, C. Peters-Lidard, M. Sivapalan, J. Sheffield, A. Wade, P. Whitehead, Hyperresolution global land surface modeling: Meeting a grand challenge for monitoring Earth's terrestrial water. *Water Resour. Res.* **47**, 1–10 (2011).
6. A. A. Ameli, C. Gabrielli, U. Morgenstern, J. J. McDonnell, Groundwater subsidy from headwaters to their parent water watershed: A combined field-modeling approach. *Water Resour. Res.* **54**, 5110–5125 (2018).
7. P. D. Brooks, J. Chorover, Y. Fan, S. E. Godsey, R. M. Maxwell, J. P. McNamara, C. Tague, Hydrological partitioning in the critical zone: Recent advances and opportunities for developing transferable understanding of water cycle dynamics. *Water Resour. Res.* **51**, 6973–6987 (2015).
8. J. Orlando, X. Comas, S. A. Hynek, H. L. Buss, S. L. Brantley, Architecture of the deep critical zone in the Río Icacos watershed (Luquillo Critical Zone Observatory, Puerto Rico) inferred from drilling and ground penetrating radar (GPR). *Earth Surf. Process. Landf.* **41**, 1826–1840 (2016).
9. W. S. Holbrook, V. Marcon, A. R. Bacon, S. L. Brantley, B. J. Carr, B. A. Flinchum, D. D. Richter, C. S. Riebe, Links between physical and chemical weathering inferred from a 65-m-deep borehole through Earth's critical zone. *Sci. Rep.* **9**, 4495 (2019).
10. T. K. Tokunaga, J. Wan, K. H. Williams, W. Brown, A. Henderson, Y. Kim, A. P. Tran, M. E. Conrad, M. Bill, R. W. H. Carroll, W. Dong, Z. Xu, A. Lavy, B. Gilbert, S. Romero, J. N. Christensen, B. Faybishenko, B. Arora, E. R. Siirila-Woodburn, R. Versteeg, J. H. Raberg, J. E. Peterson, S. S. Hubbard, Depth- and time-resolved distributions of snowmelt-driven hillslope subsurface flow and transport and their contributions to surface waters. *Water Resour. Res.* **55**, 9474–9499 (2019).
11. J. J. McDonnell, M. Sivapalan, K. Vaché, S. Dunn, G. Grant, R. Haggerty, C. Hinz, R. Hooper, J. Kirchner, M. L. Roderick, J. Selker, M. Weiler, Moving beyond heterogeneity and process complexity: A new vision for watershed hydrology. *Water Resour. Res.* **43**, 1–6 (2007).
12. R. Cassidy, J.-C. Comte, J. Nitsche, C. Wilson, R. Flynn, U. Ofterdinger, Combining multi-scale geophysical techniques for robust hydro-structural characterisation in catchments underlain by hard rock in post-glacial regions. *J. Hydrol.* **517**, 715–731 (2014).
13. J. C. Comte, U. Ofterdinger, A. Legchenko, J. Caulfield, R. Cassidy, J. A. Mézquita González, Catchment-scale heterogeneity of flow and storage properties in a weathered/fractured hard rock aquifer from resistivity and magnetic resonance surveys: Implications for groundwater flow paths and the distribution of residence times. *Geol. Soc. Spec. Publ.* **479**, 35–58 (2019).
14. J. Chen, S. S. Hubbard, D. Gaines, V. Korneev, G. Baker, D. Watson, Stochastic estimation of aquifer geometry using seismic refraction data with borehole depth constraints. *Water Resour. Res.* **46**, W11539 (2010).
15. M. B. Kowalsky, J. Chen, S. S. Hubbard, Joint inversion of geophysical and hydrological data for improved subsurface characterization. *Lead. Edge* **25**, 730–734 (2006).
16. J. Chen, S. Hubbard, J. Peterson, K. Williams, M. Fienen, P. Jardine, D. Watson, Development of a joint hydrogeophysical inversion approach and application to a contaminated fractured aquifer. *Water Resour. Res.* **42**, W06425 (2006).
17. N. Lesparre, J. F. Girard, B. Jeannot, S. Weill, M. Dumont, M. Boucher, D. Viville, M. C. Pierret, A. Legchenko, F. Delay, Magnetic resonance sounding measurements as posterior information to condition hydrological model parameters: Application to a hard-rock headwater catchment. *J. Hydrol.* **587**, 124941 (2020).
18. R. S. Anderson, S. P. Anderson, G. E. Tucker, Rock damage and regolith transport by frost: An example of climate modulation of the geomorphology of the critical zone. *Earth Surf. Process. Landf.* **38**, 299–316 (2013).
19. D. M. Rempe, W. E. Dietrich, A bottom-up control on fresh-bedrock topography under landscapes. *Proc. Natl. Acad. Sci. U.S.A.* **111**, 6576–6581 (2014).
20. J. S. Clair, S. Moon, W. S. Holbrook, J. T. Perron, C. S. Riebe, S. J. Martel, B. Carr, C. Harman, K. Singha, D. B. De Richter, Geophysical imaging reveals topographic stress control of bedrock weathering. *Science* **350**, 534–538 (2015).
21. C. S. Riebe, W. J. Hahm, S. L. Brantley, Controls on deep critical zone architecture: A historical review and four testable hypotheses. *Earth Surf. Process. Landf.* **42**, 128–156 (2017).
22. J. D. Pelletier, G. A. Barron-Gafford, H. Gutiérrez-Jurado, E. S. Hinckley, E. Istanbulluoglu, L. A. McGuire, G. Niu, M. J. Poulos, C. Rasmussen, P. Richardson, T. L. Swetnam, G. E. Tucker, Which way do you lean? Using slope aspect variations to understand Critical Zone processes and feedbacks. *Earth Surf. Process. Landf.* **43**, 1133–1154 (2018).
23. R. W. H. Carroll, J. S. Deems, R. Niswonger, R. Schumer, K. H. Williams, The importance of interflow to groundwater recharge in a snowmelt-dominated headwater basin. *Geophys. Res. Lett.* **46**, 5899–5908 (2019).
24. B. B. S. Singhal, R. P. Gupta, *Applied Hydrogeology of Fractured Rocks* (Springer Netherlands, 2010).
25. U. Ofterdinger, A. M. MacDonald, J.-C. Comte, M. E. Young, Groundwater in fractured bedrock environments: Managing catchment and subsurface resources – an introduction. *Geol. Soc. London Spec. Publ.* **479**, 1–9 (2019).
26. B. A. Flinchum, W. S. Holbrook, D. Grana, A. D. Parsekian, B. J. Carr, J. L. Hayes, J. Jiao, Estimating the water holding capacity of the critical zone using near-surface geophysics. *Hydrol. Process.* **32**, 3308–3326 (2018).

27. A. Steuer, M. Smirnova, M. Becken, M. Schiffler, T. Günther, R. Rochlitz, P. Yogeshwar, W. Mörbe, B. Siemon, S. Costabel, B. Preugschat, M. Ibs-von Seht, L. S. Zampa, F. Müller, Comparison of novel semi-airborne electromagnetic data with multi-scale geophysical, petrophysical and geological data from Schleiz, Germany. *J. Appl. Geophys.* **182**, 104172 (2020).
28. C. Kirkegaard, E. Auken, A parallel, scalable and memory efficient inversion code for very large-scale airborne electromagnetics surveys. *Geophys. Prospect.* **63**, 495–507 (2015).
29. B. Siemon, A. V. Christiansen, E. Auken, A review of helicopter-borne electromagnetic methods for groundwater exploration. *Near Surf. Geophys.* **7**, 629–646 (2009).
30. D. P. Lesmes, S. P. Friedman, in *Hydrogeophysics*, Y. Rubin, S. S. Hubbard, Eds. (Water Science and Technology Library series, Springer, 2005), pp. 87–128.
31. B. J. Minsley, J. D. Abraham, B. D. Smith, J. C. Cannia, C. I. Voss, M. T. Jorgenson, M. A. Walvoord, B. K. Wylie, L. Anderson, L. B. Ball, M. Deszcz-Pan, T. P. Wellman, T. A. Ager, Airborne electromagnetic imaging of discontinuous permafrost. *Geophys. Res. Lett.* **39**, 1–8 (2012).
32. B. J. Minsley, J. R. Rigby, S. R. James, B. L. Burton, K. J. Knierim, M. D. M. Pace, P. A. Bedrosian, W. H. Kress, Airborne geophysical surveys of the lower Mississippi Valley demonstrate system-scale mapping of subsurface architecture. *Commun. Earth Environ.* **2**, 131 (2021).
33. R. Knight, R. Smith, T. Asch, J. Abraham, J. Cannia, A. Viezzoli, G. Fogg, Mapping aquifer systems with airborne electromagnetics in the central valley of California. *Groundwater* **56**, 893–908 (2018).
34. S. Silvestri, R. Knight, A. Viezzoli, C. J. Richardson, G. Z. Anshari, N. Dewar, N. Flanagan, X. Comas, Quantification of peat thickness and stored carbon at the landscape scale in tropical Peatlands: A comparison of airborne geophysics and an empirical topographic method. *Case Rep. Med.* **124**, 3107–3123 (2019).
35. K. D. Zamudio, B. J. Minsley, L. B. Ball, "Airborne electromagnetic, magnetic, and radiometric survey, upper East River and surrounding watersheds near Crested Butte, Colorado, 2017" (U.S. Geological Survey, 2021).
36. D. E. Peterson, C. A. Finn, P. A. Bedrosian, Airborne geophysical imaging of weak Zones on Iliamna Volcano, Alaska: Implications for slope stability. *J. Geophys. Res. Solid Earth* **126**, 1–21 (2021).
37. C. A. Finn, M. Deszcz-Pan, J. L. Ball, B. J. Bloss, B. J. Minsley, Three-dimensional geophysical mapping of shallow water saturated altered rocks at Mount Baker. Washington: Implications for slope stability. *J. Volcanol. Geotherm. Res.* **357**, 261–275 (2018).
38. M. Dumont, P. A. Reninger, B. Aunay, A. Pryet, D. Jougnot, J. L. Join, L. Michon, G. Martelet, Hydrogeophysical characterization in a volcanic context from local to regional scales combining airborne electromagnetism and magnetism. *Geophys. Res. Lett.* **48**, 1–11 (2021).
39. A. A. S. Barfod, I. Møller, A. V. Christiansen, Compiling a national resistivity atlas of Denmark based on airborne and ground-based transient electromagnetic data. *J. Appl. Geophys.* **134**, 199–209 (2016).
40. J. E. Podgorski, A. G. Green, T. Kalscheuer, W. K. H. Kinzelbach, H. Horstmeyer, H. Maurer, L. Rabenstein, J. Doetsch, E. Auken, T. Ngwisanyi, G. Tshoso, B. C. Jaba, O. Ntibinyane, K. Laletsang, Integrated interpretation of helicopter and ground-based geophysical data recorded within the Okavango Delta, Botswana. *J. Appl. Geophys.* **114**, 52–67 (2015).
41. J. A. Mézquita González, J.-C. Comte, A. Legchenko, U. Ofterdinger, D. Healy, Quantification of groundwater storage heterogeneity in weathered/fractured basement rock aquifers using electrical resistivity tomography: Sensitivity and uncertainty associated with petrophysical modelling. *J. Hydrol.* **593**, 19 (2021).
42. S. S. Hubbard, K. H. Williams, D. Agarwal, J. Banfield, H. Beller, N. Bouskill, E. Brodie, R. Carroll, B. Dafflon, D. Dwivedi, N. Falco, B. Faybishenko, R. Maxwell, P. Nico, C. Steefel, H. Steltzer, T. Tokunaga, P. A. Tran, H. Wainwright, C. Varadharajan, The East River, Colorado, watershed: A mountainous community testbed for improving predictive understanding of multiscale hydrological–biogeochemical dynamics. *Vadose Zone J.* **17**, 1–25 (2018).
43. J. H. Langenheim, Vegetation and environmental patterns in the crested butte area, Gunnison County, Colorado. *Ecol. Monogr.* **32**, 249–285 (1962).
44. D. L. Gaskill, F. E. Mutschler, J. H. Kramer, J. A. Thomas, S. G. Zahony, *Geologic Map of the Gothic Quadrangle, Gunnison County, Colorado* (U.S. Geological Survey, Geologic Q., 1991).
45. H. F. Malenda, N. A. Sutfin, G. Guryan, S. Stauffer, J. C. Rowland, K. H. Williams, K. Singha, From Grain to Floodplain: Evaluating heterogeneity of floodplain hydrostatigraphy using sedimentology, geophysics, and remote sensing. *Earth Surf. Process. Landf.* **44**, 1799–1815 (2019).
46. R. W. H. Carroll, L. A. Bearup, W. Brown, W. Dong, M. Bill, K. H. Willlams, Factors controlling seasonal groundwater and solute flux from snow-dominated basins. *Hydrol. Process.* **32**, 2187–2202 (2018).
47. R. W. H. Carroll, A. H. Manning, R. Niswonger, D. Marchetti, K. H. Williams, Baseflow age distributions and depth of active groundwater flow in a snow-dominated mountain headwater basin. *Water Resour. Res.* **56**, e2020WR028161 (2020).
48. R. K. Streufert, W. Eakins, H. T. Hemborg, *RS-37 Geology and Mineral Resources of Gunnison County* (Colorado Geological Survey, Division of Minerals and Geology, Department of Natural Resources, 1999).
49. D. C. Noe, J. D. Higgins, H. W. Olsen, Steeply dipping heaving bedrock, colorado: Part 2 mineralogical and engineering properties. *Environ. Eng. Geosci.* **13**, 309–324 (2007).
50. M. A. Walvoord, P. Pegram, F. M. Phillips, M. Person, T. L. Kieft, J. K. Fredrickson, J. P. McKinley, J. B. Swenson, Groundwater flow and geochemistry in the Southeastern San Juan Basin: Implications for microbial transport and activity. *Water Resour. Res.* **35**, 1409–1424 (1999).
51. S. J. Morrison, C. S. Goodknight, A. D. Tigar, R. P. Bush, A. Gil, Naturally occurring contamination in the mancos shale. *Environ. Sci. Technol.* **46**, 1379–1387 (2012).
52. J. Wan, T. K. Tokunaga, W. Brown, A. W. Newman, W. Dong, M. Bill, C. A. Beutler, A. N. Henderson, N. Harvey-Costello, M. E. Conrad, N. J. Bouskill, S. S. Hubbard, K. H. Williams, Bedrock weathering contributes to subsurface reactive nitrogen and nitrous oxide emissions. *Nat. Geosci.* **14**, 217–224 (2021).
53. T. L. Stephens, R. J. Walker, D. Healy, A. Bubeck, R. W. England, Mechanical models to estimate the paleostress state from igneous intrusions. *Solid Earth* **9**, 847–858 (2018).
54. N. S. Christensen, D. P. Lettenmaier, A multimodel ensemble approach to assessment of climate change impacts on the hydrology and water resources of the Colorado River Basin. *Hydrol. Earth Syst. Sci.* **11**, 1417–1434 (2007).
55. L. M. Foster, K. H. Williams, R. M. Maxwell, Resolution matters when modeling climate change in headwaters of the Colorado River. *Environ. Res. Lett.* **15**, 104031 (2020).
56. K. H. Williams, A. Newman, Shale drilling field notes, lithologic descriptions, and core photographs of wells PLM5, PLM8, GUM1, and GLS1 at the East River Watershed, Colorado (Watershed Function SFA, ESS-DIVE repository, 2020).
57. S. Uhlemann, B. Carr, B. Dafflon, K. Williams, Geophysical borehole logging data of wells ER-GLS1, ER-GUM1, ER-PLM7, and ER-PLM8 at the East River Watershed, Colorado (Watershed Function SFA, ESS-DIVE repository, 2020).
58. W. Dong, C. Beutler, W. Brown, A. Newman, R. Versteeg, K. H. Williams, Cation Data for the East River Watershed, Colorado (Watershed Function SFA, ESS-DIVE repository, 2020).
59. K. H. Williams, C. Beutler, W. Brown, A. Newman, R. Versteeg, Anion Data for the East River Watershed, Colorado (Watershed Function SFA, ESS-DIVE repository, 2020).
60. B. C. Sams, Contact metamorphism of the Mancos shale: Impacts on solute release and weatherability in the East River Valley, Gothic, CO, M.Sc. thesis, Colorado School of Mines, Golden, CO (2018).
61. K. Keating, R. Knight, A laboratory study of the effect of magnetite on NMR relaxation rates. *J. Appl. Geophys.* **66**, 188–196 (2008).
62. A. A. Behroozmand, K. Keating, E. Auken, A review of the principles and applications of the NMR technique for near-surface characterization. *Surv. Geophys.* **36**, 27–85 (2015).
63. N. Foged, E. Auken, A. V. Christiansen, K. I. Sørensen, Test-site calibration and validation of airborne and ground-based TEM systems. *Geophysics* **78**, E95–E106 (2013).
64. G. E. Archie, The electrical resistivity log as an aid in determining some reservoir characteristics. *Pet. Trans. AIME.* **146**, 54–62 (1942).
65. K. Singha, F. D. Day-Lewis, T. Johnson, L. D. Slater, Advances in interpretation of subsurface processes with time-lapse electrical imaging. *Hydrol. Process.* **29**, 1549–1576 (2015).
66. W. Dershowitz, I. Miller, Dual porosity fracture flow and transport. *Geophys. Res. Lett.* **22**, 1441–1444 (1995).
67. J. Wu, T. Goto, K. Koike, Estimating fractured rock effective permeability using discrete fracture networks constrained by electrical resistivity data. *Eng. Geol.* **289**, 106178 (2021).
68. A. Kirkby, G. Heinson, L. Krieger, Relating permeability and electrical resistivity in fractures using random resistor network models. *J. Geophys. Res. Solid Earth* **121**, 1546–1564 (2016).
69. A. Shahbazi, A. Saeidi, R. Chesnaux, A review of existing methods used to evaluate the hydraulic conductivity of a fractured rock mass. *Eng. Geol.* **265**, 105438 (2020).
70. N. Falco, H. Wainwright, B. Dafflon, E. Léger, J. Peterson, H. Steltzer, C. Wilmer, J. C. Rowland, K. H. Williams, S. S. Hubbard, Investigating microtopographic and soil controls on a mountainous meadow plant community using high-resolution remote sensing and surface geophysical data. *J. Geophys. Res. Biogeosci.* **124**, 1618–1636 (2019).
71. D. E. J. Hobley, J. M. Adams, S. S. Nudurupati, E. W. H. Hutton, N. M. Gasparini, E. Istanbulluoglu, G. E. Tucker, Creative computing with Landlab: An open-source toolkit for building, coupling, and exploring two-dimensional numerical models of Earth-surface dynamics. *Earth Surf. Dyn.* **5**, 21–46 (2017).
72. N. Falco, A. Balde, I. Breckheimer, E. Brodie, P. Brodrick, D. Chadwick, J. Chen, B. Dafflon, A. Henderson, J. Lamb, K. Maher, L. Kueppers, H. Steltzer, H. Wainwright, K. Williams, S. Hubbard, Plant species distribution within the Upper Colorado River Basin estimated by using hyperspectral and LiDAR airborne data (Watershed Function SFA, ESS-DIVE repository, 2020).
73. P. Geurts, D. Ernst, L. Wehenkel, Extremely randomized trees. *Mach. Learn.* **63**, 3–42 (2006).

74. B. A. Clarke, D. W. Burbank, Bedrock fracturing, threshold hillslopes, and limits to the magnitude of bedrock landslides. *Earth Planet. Sci. Lett.* **297**, 577–586 (2010).
75. C. P. Gillin, S. W. Bailey, K. J. McGuire, J. P. Gannon, Mapping of hydropedologic spatial patterns in a steep headwater catchment. *Soil Sci. Soc. Am. J.* **79**, 440–453 (2015).
76. W. J. Hahm, C. S. Riebe, C. E. Lukens, S. Araki, Bedrock composition regulates mountain ecosystems and landscape evolution. *Proc. Natl. Acad. Sci.* **111**, 3338–3343 (2014).
77. H. Liu, J. Dai, C. Xu, J. Peng, X. Wu, H. Wang, Bedrock-associated belowground and aboveground interactions and their implications for vegetation restoration in the karst critical zone of subtropical Southwest China. *Prog. Phys. Geogr.* **45**, 030913332094986 (2020).
78. Z. Jiang, H. Liu, H. Wang, J. Peng, J. Meersmans, S. M. Green, T. A. Quine, X. Wu, Z. Song, Bedrock geochemistry influences vegetation growth by regulating the regolith water holding capacity. *Nat. Commun.* **11**, 2392 (2020).
79. D. R. Montgomery, Slope distributions, threshold hillslopes, and steady-state topography. *Am. J. Sci.* **301**, 432–454 (2001).
80. Q. Yan, H. Wainwright, B. Dafflon, S. Uhlemann, C. I. Steefel, N. Falco, J. Kwang, S. S. Hubbard, A hybrid data–model approach to map soil thickness in mountain hillslopes. *Earth Surf. Dyn.* **9**, 1347–1361 (2021).
81. J. R. Hamilton, Incipient metamorphism and the organic geochemistry of the Mancos Shale near Crested Butte, Colorado, M.Sc. thesis, Rice University, Houston, TX (1972).
82. J. R. Delsman, E. S. van Baaren, B. Siemon, W. Dabekaussen, M. C. Karaoulis, P. S. Pauw, T. Vermaas, H. Bootsma, P. G. B. de Louw, J. L. Gunnink, C. W. Dubelaar, A. Menkovic, A. Steuer, U. Meyer, A. Revil, G. H. P. Oude Essink, Large-scale, probabilistic salinity mapping using airborne electromagnetics for groundwater management in Zeeland, the Netherlands. *Environ. Res. Lett.* **13**, 084011 (2018).
83. A. Miltenberger, S. Uhlemann, T. Mukerji, K. Williams, B. Dafflon, L. Wang, H. Wainwright, Probabilistic evaluation of geoscientific hypotheses with geophysical data: Application to electrical resistivity imaging of a fractured bedrock zone. *J. Geophys. Res. Solid Earth* **126**, e2021JB021767 (2021).
84. B. Arora, M. Burrus, M. Newcomer, C. I. Steefel, R. W. H. Carroll, D. Dwivedi, W. Dong, K. H. Williams, S. S. Hubbard, Differential C-Q analysis: A new approach to inferring lateral transport and hydrologic transients within multiple reaches of a mountainous headwater catchment. *Front. Water* **2**, 24 (2020).
85. D. Walsh, P. Turner, E. Grunewald, H. Zhang, J. J. Butler, E. Reboulet, S. Knobbe, T. Christy, J. W. Lane, C. D. Johnson, T. Munday, A. Fitzpatrick, A small-diameter nmr logging tool for groundwater investigations. *Groundwater* **51**, 914–926 (2013).
86. K. Dlubac, R. Knight, Y.-Q. Song, N. Bachman, B. Grau, J. Cannia, J. Williams, Use of NMR logging to obtain estimates of hydraulic conductivity in the High Plains aquifer, Nebraska, USA. *Water Resour. Res.* **49**, 1871–1886 (2013).
87. R. A. Freeze, J. A. Cherry, *Groundwater* (Prentice-Hall Inc., 1979).
88. P. M. Quinn, B. L. Parker, J. A. Cherry, Using constant head step tests to determine hydraulic apertures in fractured rock. *J. Contam. Hydrol.* **126**, 85–99 (2011).
89. T. C. Johnson, R. J. Versteeg, A. Ward, F. D. Day-Lewis, A. Revil, Improved hydrogeophysical characterization and monitoring through parallel modeling and inversion of time-domain resistivity andinduced-polarization data. *Geophysics* **75**, WA27–WA41 (2010).
90. E. Auken, A. V. Christiansen, C. Kirkegaard, G. Fiandaca, C. Schamper, A. A. Behroozmand, A. Binley, E. Nielsen, F. Effersø, N. B. Christensen, K. Sørensen, N. Foged, G. Vignoli, An overview of a highly versatile forward and stable inverse algorithm for airborne, ground-based and borehole electromagnetic and electric data. *Explor. Geophys.* **46**, 223–235 (2015).
91. G. Fiandaca, L. M. Madsen, P. K. Maurya, Re-parameterisations of the Cole-Cole model for improved spectral inversion of induced polarization data. *Near Surf. Geophys.* **16**, 385–399 (2018).
92. A. V. Christiansen, E. Auken, A global measure for depth of investigation. *Geophysics* **77**, WB171–WB177 (2012).
93. G. Varoquaux, L. Buitinck, G. Louppe, O. Grisel, F. Pedregosa, A. Mueller, Scikit-learn. *GetMobile Mob. Comput. Commun.* **19**, 29–33 (2015).

Acknowledgments: We would like to thank P. McClure for help during the acquisition of the near-surface geophysical data and K. Keating for sharing insight into the NMR data and for sharing a processing code. Any use of trade, firm, or product names is for descriptive purposes only and does not imply endorsement by the U.S. government. **Funding:** We acknowledge support from the Watershed Function Scientific Focus Area funded by the U.S. Department of Energy, Office of Science, Office of Biological and Environmental Research under award no. DE-AC02-05CH11231. B.M. and K.Z. acknowledge support from the U.S. Geological Survey Mineral Resources Program. **Author contributions:** S.U., B.D., C.U., and K.H.W. assisted in data collection (borehole and near-surface geophysical data), study design, and data analysis. S.U. led the data analysis and manuscript preparation. B.M. and B.C. led the acquisition of the airborne and borehole geophysical data, respectively. K.Z. and N.F. processed and analyzed the AEM and remote sensing data, respectively. S.H. acquired funding for this study. All authors contributed to the manuscript. **Competing interests:** The authors declare that they have no competing interests. **Data and materials availability:** The borehole geophysical logging data, as well as the core photographs and the near-surface geophysical data, can be obtained from (*57*) and (*56*). The LiDAR and vegetation datasets can be accessed at (*72*). The AEM data are published in (*35*). All data needed to evaluate the conclusions in the paper are present in the paper and/or the Supplementary Materials.

Submitted 3 May 2021
Accepted 3 February 2022
Published 23 March 2022
10.1126/sciadv.abj2479